

Predictive Control over Charge Density in the Two-Dimensional Electron Gas at the Polar-Nonpolar NdTiO₃/SrTiO₃ Interface

Peng Xu,¹ Yilikal Ayino,² Christopher Cheng,¹ Vlad S. Pribiag,² Ryan B. Comes,³ Peter V. Sushko,³ Scott A. Chambers,³ and Bharat Jalan^{1,*}

¹Department of Chemical Engineering and Materials Science, University of Minnesota, Minneapolis, Minnesota 55455, USA

²School of Physics and Astronomy, University of Minnesota, Minneapolis, Minnesota 55455, USA

³Physical & Computational Sciences Directorate, Pacific Northwest National Laboratory, Richland, Washington 99352, USA

(Received 29 March 2016; published 1 September 2016)

Through systematic control of the Nd concentration, we show that the carrier density of the two-dimensional electron gas (2DEG) in SrTiO₃/NdTiO₃/SrTiO₃(001) can be modulated over a wide range. We also demonstrate that the NdTiO₃ in heterojunctions without a SrTiO₃ cap is degraded by oxygen absorption from air, resulting in the immobilization of donor electrons that could otherwise contribute to the 2DEG. This system is, thus, an ideal model to understand and control the insulator-to-metal transition in a 2DEG based on both environmental conditions and film-growth processing parameters.

DOI: 10.1103/PhysRevLett.117.106803

The debate over mechanisms of electronic phenomena at polar-nonpolar interfaces is part of a larger effort to understand emergent phenomena in complex oxides, a class of materials that exhibits an exceedingly wide range of properties [1–6]. Polar-nonpolar interfaces can be categorized as those with the same *B*-site cation and those with different *B*-site cations. The former include RTiO₃ on SrTiO₃ where *R* = La, Gd, and Nd. A special subset of the latter is that with a nonreducible *B*-site cation, the most widely studied being LaAlO₃ (LAO) on SrTiO₃ (STO). However, consensus has not yet been reached concerning the mechanism(s) of interfacial conduction, which has been linked to nonstoichiometry in the LAO film [1–5]. Starting with the earliest observations, it has been hypothesized that conductivity arises from an electronic reconstruction (ER) to alleviate the “polar catastrophe” which accompanies the formation of an abrupt interface [7]. Extrinsic factors, such as unintentional doping via cation intermixing and oxygen vacancy generation, have also been considered in light of the actual, as opposed to idealized properties of the interface [1,3,8–12]. The debate over conduction mechanism(s) has been further fueled by the fact that ER predicts a carrier concentration of 0.5 electrons per unit cell ($e^-/\text{u.c.}$) ($3.3 \times 10^{14} \text{ cm}^{-2}$), whereas virtually all experiments carried out to date reveal carrier densities an order of magnitude lower unless abundant oxygen vacancies are present in the STO, in which case, the carrier density is larger than the ER prediction.

In RTiO₃/STO the common *B*-site cation leads to a symmetrical interface $(\text{Ti}^{4+}\text{O}_2^-)^0(\text{R}^{3+}\text{O}_2^-)+(\text{Ti}^{3+}\text{O}_2^-)^-$, independent of growth sequence. As a result, as little as 1 u.c. of RTiO₃ on TiO₂-terminated STO has been predicted to act as a δ -doping layer which would provide 0.5 $e^-/\text{u.c.}$ per interface via ER [13]. However, previous work has found that for 1 u.c. RTiO₃, the carrier concentration was

substantially lower than the value expected from the ER model [13,14]. To date MBE-grown NdTiO₃/STO (NTO/STO) [15] and GdTiO₃/STO (GTO/STO) [16,17] exhibit a carrier density of 0.5 $e^-/\text{u.c.}$ per interface only for ≥ 2 –3 u.c. RTiO₃ layers, in addition to a STO capping layer. In contrast, the conductivity threshold for NTO/STO heterojunctions without a STO capping layer is much higher (8 u.c.) [15].

In this Letter, we present a unified picture of the origin of the two-dimensional electron gas (2DEG) in NTO/STO(001). NTO is a Mott insulator with a gap of 0.8 eV. Transport data reveal that bulk, single-crystal NTO exhibits semiconducting behavior with an activation energy of ~ 0.084 eV [18]. Additionally, magnetic susceptibility measurements yield Curie-Weiss behavior consistent with d^1 moments localized on Ti sites and conduction by electron or small polaron hopping [19]. The present results shed light on the fundamental properties of polar-nonpolar heterostructures and provide a novel yet simple route for their control. We demonstrate that STO/1 u.c. NTO/STO(001) exhibits metallic conductivity with a carrier density equal to 0.5 $e^-/\text{u.c.}$ We then show why uncapped NTO/STO(001) exhibits a much higher conductivity threshold than STO-capped specimens. Finally, we demonstrate that the carrier density in STO/ ≥ 2 u.c. NTO/STO(001) can be tuned through the controlled introduction of Nd vacancies (V_{Nd}). V_{Nd} have the effect of increasing the Ti formal charge from 3+ to 4+ via localized hole doping, thereby modulating the carrier concentration.

All STO/NTO/STO heterostructures were prepared using hybrid molecular beam epitaxy (MBE) [20]. Figure 1 shows the temperature dependence of the sheet resistance (R_s) for 8 u.c. STO/1 u.c. NTO/8 u.c. STO/LSAT(001). R_s first decreases with decreasing temperature and then increases below ~ 70 K. Such an upturn is

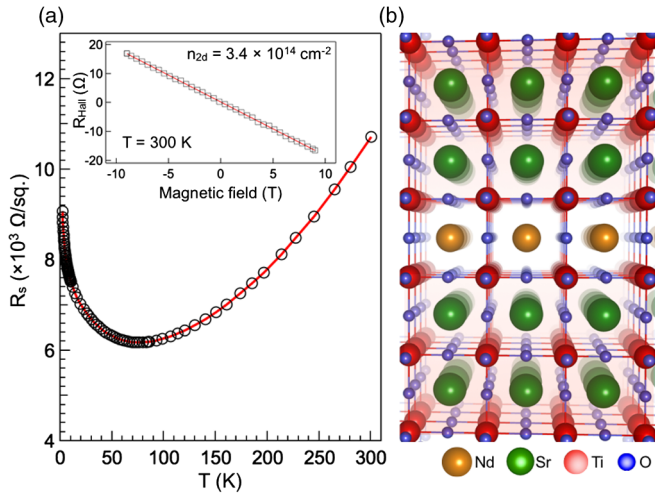


FIG. 1. (a) Temperature-dependent resistivity for 8 u.c. STO/1 u.c. NTO/8 u.c. STO/LSAT(001). Inset shows the Hall data revealing n -type behavior and a carrier concentration of $0.5 e^-/\text{u.c.}$ (b) A structural model of the 1 u.c. NTO layer sandwiched between STO layers.

widely ascribed to weak localization [43]. The inset shows the Hall resistance at 300 K as a function of magnetic field; the slope indicates n -type conduction with a carrier density of $3.4 \times 10^{14} \text{ cm}^{-2}$. Interestingly, the carrier density is exactly half the value expected from electronic reconstruction by a single monolayer of NdO [13].

Next, we examine the role of the STO capping layer on interfacial conductivity. Although capped STO/NTO/STO heterojunctions are conductive for ≥ 1 u.c. NTO, the conductivity threshold is 8 u.c. if no STO cap is present [15]. Additionally, prolonged air exposure converts uncapped conductive samples of NTO/STO into insulators even if the NTO thickness is greater than 8 u.c. As described below, our combined experimental and theoretical results suggest that this transition is caused by oxygen absorption at air-exposed NTO film surfaces, leading to oxidation of Ti^{3+} cations which quenches polarization doping of the STO. Our first-principles calculations show that stoichiometric NTO readily incorporates interstitial oxygen (O_{int}) and predict that NTO absorbs oxygen until a composition of $\text{NdTiO}_{3.5}$ is reached (see the Supplemental Material [20], Fig. S3). This result is supported by the fact that the ratio of O $1s$ and Ti $2p_{3/2}$ peak areas in air-exposed NTO(001) is 46% larger than that for air-exposed STO(001). Charge population analysis shows that incorporation of a single extra oxygen atom results in the conversion of two Ti^{3+} ions into Ti^{4+} ions, while the extra oxygen, which occupies interstitial sites, acquires an atomic charge indistinguishable from that of the host lattice O^{2-} ions. Accordingly, the occupied Ti $3d$ -derived lower Hubbard band in stoichiometric NTO is depleted while the width of the O $2p$ valence band increases with increasing excess oxygen concentration. As a result, the NTO layer is

unable to dope the adjacent STO layer. It is only when the NTO film is sufficiently thick and kinetic limitations prevent oxygen from reaching the buried layers that NTO is able to dope STO.

These conclusions are fully supported by our experimental data. We compare in Fig. 2(a) x-ray photoelectron spectra (XPS) for a 10 nm NTO film with those for bulk Nb-doped $\text{SrTiO}_3(001)$. To facilitate comparison, we have applied a rigid shift to the NTO binding energies scales such that the lattice O $1s$ peak aligns with that for Nb:STO(001). Inspection of the Ti $2p_{3/2}$ spectrum for NTO reveals a complex line shape whereas the spectrum for STO consists of a sharp singlet. The intense feature in the NTO spectrum at 458.1 eV is shifted 0.6 eV to lower binding energy from the single peak in the n -STO spectrum. This value is far less than the ~ 2 eV shift observed in going from Ti^{4+} to Ti^{3+} in STO doped with high quantities of substitutional La or Nb or

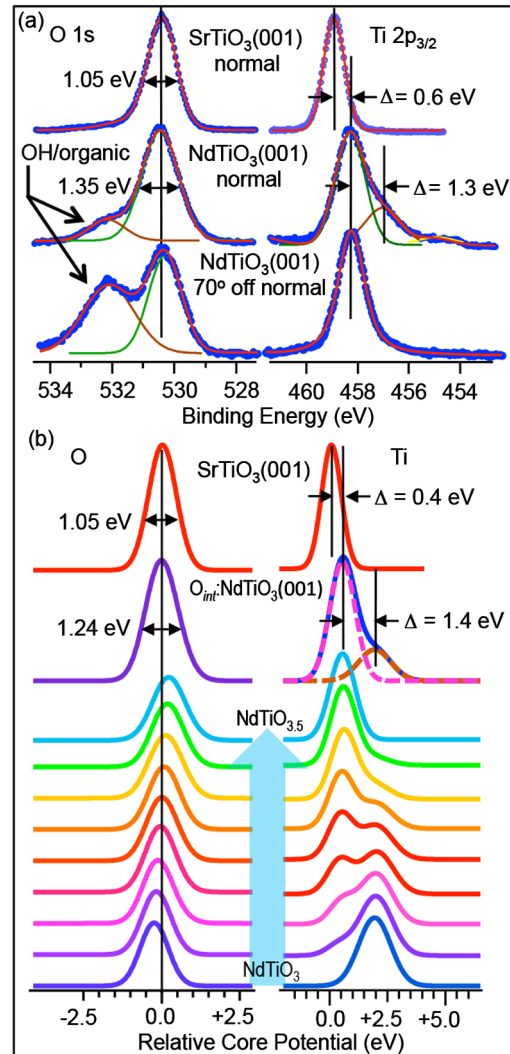


FIG. 2. (a) Experimental core-level x-ray photoelectron spectra and (b) theoretical core potentials for 10 nm NTO/LSAT(001) and bulk n -STO(001).

O vacancies [44–46]. We assign this feature to Ti^{4+} in NTO within the layer containing excess oxygen, as explained below. A second significant difference between NTO and STO is found in the O $1s$ spectra, also seen in Fig. 2(a). The full widths at half maximum (FWHM) are 1.35 eV for NTO and 1.05 eV for STO.

Low-angle XPS measurements [Fig. 2(a)] show that the near-surface region of the NTO film consists entirely of Ti^{4+} . After proper scaling, taking the difference of spectra measured along the surface normal and 70° off normal reveals that the deeper NTO layers consist entirely of the weaker peak seen in Fig. 2(a) at 456.8 eV with a broad shoulder at ~ 455 eV (see the Supplemental Material [20], Fig. S4). These results are consistent with a concentration profile for O_{int} which transforms virtually all Ti cations in the near-surface region to Ti^{4+} and then falls off with increasing depth, leaving the Ti^{3+} cations at the bottom of the XPS probe depth (~ 5 nm). To test these assignments against first-principles simulations, we have calculated the on-site electrostatic potential for all O and Ti ions in $\text{NdTiO}_{3+\delta}$ as a function of δ ($\delta = 0.0 \rightarrow 0.5$), which corresponds to the supercell composition $\text{Nd}_{16}\text{Ti}_{16}\text{O}_{48+n}$ ($n = 0 \rightarrow 8$). At $n = 8$, enough oxygen has been added to convert all Ti^{3+} to Ti^{4+} . Since both the O $1s$ and Ti $2p$ atomic orbitals are within the projected augmented wave pseudopotentials, variations in the on-site electrostatic potentials are expected to match changes in the associated binding energy shifts, assuming the effects of core-hole screening are independent of δ . The results are shown in the Supplemental Material [20], Figs. S5 and S6. The difference between on-site potentials at the Ti^{4+} and Ti^{3+} sites in NTO and the widths of the potential distributions show little dependence on the choice of the lattice parameters. Core potential distributions at the O sites (viz., theoretical O $1s$ spectra) were constructed by broadening each data point with a Gaussian of the same width as that measured for O $1s$ in STO (1.05 eV). We then averaged these spectra for all nine oxygen concentrations to represent the gradient within the probe depth of the actual specimen. The result is shown at the top of Fig. 2(b) and is labeled $\text{O}_{\text{int}}:\text{NTO}$. The family of theoretical spectra for $\text{Nd}_{16}\text{Ti}_{16}\text{O}_{48+n}$, ($n = 0 \rightarrow 8$) is shown in the bottom part of Fig. 2(b). Likewise, the potentials for each Ti^{4+} and Ti^{3+} cation in NTO were broadened by convolving with Gaussians of the same widths as those measured experimentally [Fig. 2(a)] to construct theoretical Ti $2p$ spectra. In the absence of detailed information on the O_{int} concentration profile, we simulated the experimental spectrum by averaging the theoretical spectra for the end members ($\text{NdTiO}_{3.0}$ and $\text{NdTiO}_{3.5}$) with weighting factors of 0.25 and 0.75, respectively. These spectra are also shown at the top of Fig. 2(b). Finally, we aligned the theoretical spectra in the same way as we did the experimental spectra; the energy scale was shifted so the O peak energy for $\text{O}_{\text{int}}:\text{NTO}$ matches that for STO.

For both Ti and O, we find excellent agreement between theoretical and experimental spectra for $\text{O}_{\text{int}}:\text{NTO}(001)$. The increase in O $1s$ FWHM from STO to $\text{O}_{\text{int}}:\text{NTO}$ attributed to lattice distortions is well captured by theory; the theoretical FWHM is 1.24 eV compared to 1.35 eV in experiment. Similarly, the calculated energy difference between Ti^{4+} in STO and Ti^{4+} in NTO (0.4 eV) agrees well with experiment (0.6 eV), as does the chemical shift between Ti^{4+} and Ti^{3+} in NTO (1.4 eV compared to 1.3 eV). These results shed light on spectral interpretation in recent literature on the Ti $2p$ binding energies of RTiO_3 epitaxial films [47,48] and underscore that the overall electrostatic environment in addition to formal cation valence determine initial-state effects in XPS.

The fact that the charge available in NTO for polarization doping of adjacent STO layers can be immobilized by conversion of Ti^{3+} to Ti^{4+} via addition of oxygen suggests that there may be other more controllable ways of tuning the carrier density in adjacent STO layers. One approach is the creation of Nd vacancies (V_{Nd}). We hypothesize that the NTO lattice will compensate for each V_{Nd} by generating three holes that localize on three Ti^{3+} cations, thereby

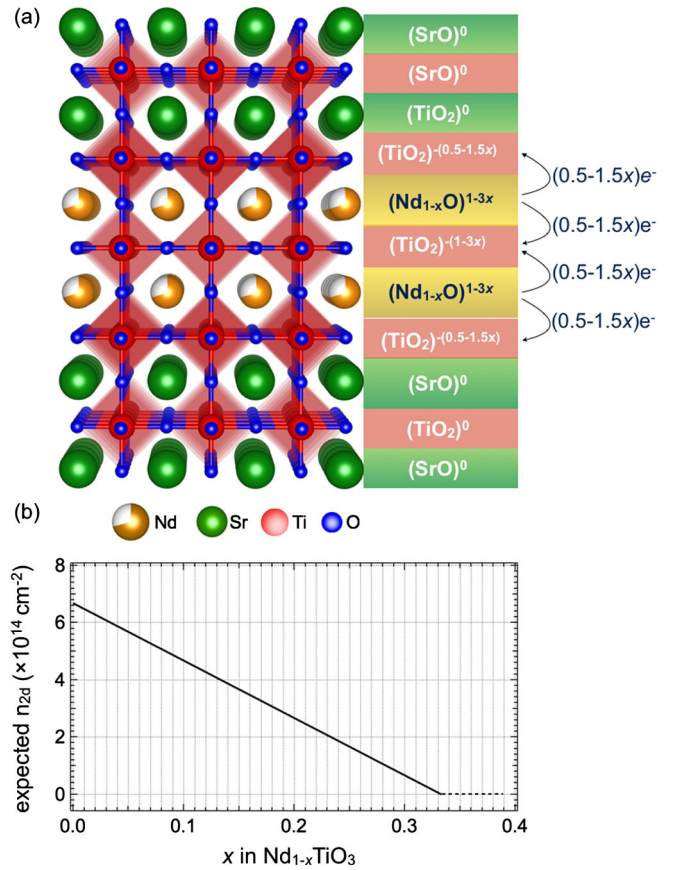


FIG. 3. (a) Schematic illustration of an electronic reconstruction model for a multilayer of $\text{Nd}_{1-x}\text{TiO}_3$ sandwiched between layers of STO. (b) The expected charge density (n_{2d}) based on the electronic reconstruction model as a function of x .

reducing the available charge that can be transferred to STO via polarization doping [49]. We show in Fig. 3(a) a schematic of the ER model for 2 u.c. of the $\text{Nd}_{1-x}\text{TiO}_3$ layer sandwiched between SrTiO_3 layers. Each $(\text{Nd}_{1-x}\text{O})^{1-3x}$ layer should electron dope the adjacent STO layer, resulting in a net charge of $0.5-1.5x e^-/\text{u.c.}$ per interface. Accordingly, the total carrier density (n_{2d}) at both interfaces should be

$$n_{2d} = 6.69 \times 10^{14}(1-3x) \text{ cm}^{-2}. \quad (1)$$

For ≥ 2 u.c. of $\text{Nd}_{1-x}\text{TiO}_3$, the carrier density is expected to decrease linearly from $6.69 \times 10^{14} \text{ cm}^{-2}$ with x and reach zero at $x = 1/3$, as seen in Fig. 3(b).

In order to systematically investigate the effect of V_{Nd} on carrier density, we prepared a series of 8 u.c. STO/2 u.c. $\text{Nd}_{1-x}\text{TiO}_3/8$ u.c. STO/LSAT(001) heterostructures for different x (see the Supplemental Material [20], Fig. S2 for characterization data). The value of x was controlled by varying the titanium tetraisopropoxide (TTIP):Nd beam equivalent pressure (BEP) ratio at a fixed TTIP BEP. Note that TTIP also supplies the oxygen, so the oxygen flux was also kept fixed. Figure 4 shows R_s vs T , along with n_{2d} and electron mobility (μ) at room temperature as a function of the Ti:Nd BEP ratio. $R_s(T)$ increases with the Ti:Nd BEP ratio, in agreement with our prior work [21]. We also observe a monotonic decrease in n_{2d} that becomes nearly constant at $\sim 3 \times 10^{13} \text{ cm}^{-2}$ for a Ti:Nd BEP ratio in excess of 40. Significantly, the overall trend is very similar to the behavior expected based on our model [Fig. 3(b)] and the 2DEG density is $\sim 7 \times 10^{14} \text{ cm}^{-2}$ ($0.5 e^-/\text{u.c.}$ per interface) for the stoichiometric composition (Ti:Nd BEP ratio=7.7).

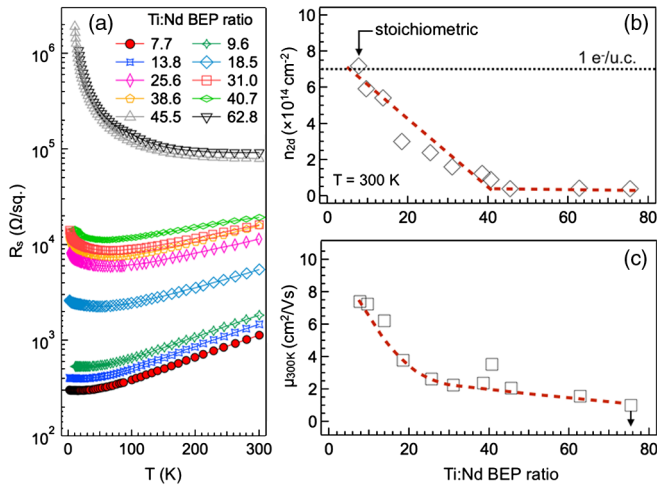


FIG. 4. (a) Temperature-dependent resistivity of 8 u.c. STO/2 u.c. NTO/8 u.c. STO/LSAT(001) as a function of the Ti:Nd BEP ratio used for NTO growth. (b) Room-temperature two-dimensional carrier concentrations and (c) electron mobility as a function of the Ti:Nd BEP ratio used during NTO growth. Note that the Ti and O fluxes were kept fixed.

Given that the V_{Nd} concentration was controlled by changing the Nd flux at fixed TTIP (and, therefore, oxygen) flux, the Ti:Nd BEP ratio (r_{BEP}) and x can be related by an empirical relationship

$$x = \frac{r_{\text{BEP}} - r_{\text{BEP}}^{\text{stoich}}}{\alpha}, \quad (2)$$

where α is a proportionality constant and $r_{\text{BEP}}^{\text{stoich}} = 7.7$, which is the Ti:Nd BEP ratio for stoichiometric NTO. Inserting Eq. (2) into Eq. (1), we express n_{2d} in terms of r_{BEP} , and α as

$$n_{2d} = 6.69 \times 10^{14} \left[1 - \frac{3}{\alpha}(r_{\text{BEP}} - 7.7) \right] \text{ cm}^{-2}. \quad (3)$$

Using Eq. (3), we fit the linearly decreasing portion of the data in Fig. 3(b) and obtained a value of $\alpha = 107$. From Eq. (2), x can be determined as a function of r_{BEP} , providing a relationship between the growth parameters and the V_{Nd} concentration. Using this expression, we calculate x at the critical value of the Ti:Nd BEP ratio ($r_{\text{BEP}} = 42$) where n_{2d} becomes constant. We obtain a value of 0.32, the same as that predicted by our model [Fig. 3(b)]. This result not only provides direct evidence for ER being operative but also yields a simple, direct relationship between growth parameters and the 2DEG, thereby enabling predictive control over carrier density.

Our data do not allow us to say if V_{Nd} -induced small-hole polaron transport [50,51] within the $\text{Nd}_{1-x}\text{TiO}_3$ is operative. However, due to the low mobility, the holes are not expected to contribute to the measured Hall voltage; hence, the latter is dominated by electrons in the STO [15]. The other candidate compensation mechanism is V_{O} creation. If V_{O} generation occurred, the Nd-deficient NTO phase would be $\text{Nd}_{1-x}\text{TiO}_{3-\delta}$. However, inasmuch as V_{O} is a double donor, n_{2d} would then be given by $(1-3x+2\delta) e^-/\text{u.c.}$ In this scenario, δ , x , n_{2d} would be related to r_{BEP} by a more complex relationship than Eq. (3). Additionally, the value of δ would need to be nearly zero to yield the observed x value at which the carrier density becomes $1 e^-/\text{u.c.}$ ($x = 0$) or zero ($x = 1/3$). The good agreement between our data and the simple linear dependence of Eq. (3) suggests that the V_{O} creation mechanism is not relevant and that the V_{Nd} mechanism dominates.

As a further check of our model, we use XPS to relate the x values inferred from carrier densities to actual V_{Nd} concentrations. In order to do so, we compare core-level intensities and line shapes for representative uncapped 10 nm films of stoichiometric NTO and Nd-deficient NTO grown directly on LSAT for which $x = \sim 0.08$ based on the r_{BEP} value. Assuming no change in the electron attenuation length and a uniform distribution of V_{Nd} , x should be given by the peak area ratio of any Nd core level (e.g., $A_{\text{Nd}_{1-x}\text{TiO}_3}/A_{\text{NdTiO}_3}$). However, for 10 nm films

without a STO cap and with a large x (0.08), the NTO film appears to have different surface composition which complicates the analysis. As a result, the value of x given by $A_{\text{Nd}1-x\text{TiO}_3}/A_{\text{NdTiO}_3}$ is 0.13 (see the Supplemental Material [20], Figs. S7–S9 and associated discussion). The Ti $2p$ core-level spectra show that the near-surface region of the Nd-deficient film is enriched in Ti^{4+} more than expected based on the concentration of V_{Nd} compared to the stoichiometric film, suggesting Ti^{4+} -containing secondary phase formation. This result is consistent with the x value being overestimated. Nevertheless, these data do allow us to qualitatively conclude that reducing r_{BEP} increases V_{Nd} without introducing V_{O} . Our transport measurements combined with the XPS confirm electronic reconstruction as the mechanism of carrier generation and provide a unique pathway for predictive control over the 2D carrier density via manipulating the formal charge of Ti.

In summary, we show that $\text{NdTiO}_3/\text{SrTiO}_3$ heterostructures constitute an ideal test bed for understanding electronic reconstruction at polar-nonpolar interfaces and for exploring how such systems might be used in all-oxide 2DEG-based transistors. The combination of controlled MBE growth and detailed characterization (including expanded understanding of transition metal core-level binding energies and transport) allows us to understand, tune, and predict the properties of a very promising materials system, the study of which settles some long-standing issues concerning the true characteristics of the polar discontinuity as it exists at oxide heterojunctions.

The authors thank Professor Andre Mkhoyan for helpful discussions. This work at the University of Minnesota was supported primarily by the AFOSR young investigator program (Grant No. FA9550-16-1-0205) and in part by the UMN MRSEC under Grant No. DMR-1420013. We also acknowledge use of facilities at the UMN Characterization Facility and the Nanofabrication Center. The XPS work and computational modeling at PNNL was supported by the U.S. Department of Energy, Office of Science, Division of Materials Sciences and Engineering under Award No. 10122. R. C. was supported by the Linus Pauling Distinguished Post-Doctoral Fellowship at Pacific Northwest National Laboratory (PNNL LDRD Grant No. PN13100/2581). The PNNL work was performed in the Environmental Molecular Sciences Laboratory, a national scientific user facility sponsored by the Department of Energy's Office of Biological and Environmental Research and located at PNNL.

*bjalan@umn.edu

- [1] M. P. Warusawithana, C. Richter, J. A. Mundy, P. Roy, J. Ludwig, S. Paetel, T. Heeg, A. A. Pawlicki, L. F. Kourkoutis, M. Zheng, M. Lee, B. Mulcahy, W. Zander, Y. Zhu, J. Schubert, J. N. Eckstein, D. A. Muller, C. S. Hellberg, J. Mannhart, and D. G. Schlom, *Nat. Commun.* **4**, 2351 (2013).
- [2] C. Weiland, G. E. Sterbinsky, A. K. Rumaiz, C. S. Hellberg, J. C. Woicik, S. Zhu, and D. G. Schlom, *Phys. Rev. B* **91**, 165103 (2015).
- [3] E. Breckenfeld, N. Bronn, J. Karthik, A. R. Damodaran, S. Lee, N. Mason, and L. W. Martin, *Phys. Rev. Lett.* **110**, 196804 (2013).
- [4] L. Yu and A. Zunger, *Nat. Commun.* **5**, 5118 (2014).
- [5] D. G. Schlom and J. Mannhart, *Nat. Mater.* **10**, 168 (2011).
- [6] Y. Tokura and H. Y. Hwang, *Nat. Mater.* **7**, 694 (2008).
- [7] A. Ohtomo and H. Y. Hwang, *Nature (London)* **427**, 423 (2004).
- [8] S. A. Chambers, in *Hard X-Ray Photoelectron Spectroscopy (HAXPES)*, edited by J. Woicik (Springer, Berlin, 2015).
- [9] S. A. Chambers, M. H. Engelhard, V. Shutthanandan, Z. Zhu, T. C. Droubay, L. Qiao, P. V. Sushko, T. Feng, H. D. Lee, and T. Gustafsson, *Surf. Sci. Rep.* **65**, 317 (2010).
- [10] A. Kalabukhov, R. Gunnarsson, J. Borjesson, E. Olsson, T. Claesson, and D. Winkler, *Phys. Rev. B* **75**, 121404 (2007).
- [11] W. Siemons, G. Koster, H. Yamamoto, W. A. Harrison, G. Lucovsky, T. H. Geballe, D. H. A. Blank, and M. R. Beasley, *Phys. Rev. Lett.* **98**, 196802 (2007).
- [12] A. Brinkman, M. Huijben, M. Van Zalk, J. Huijben, U. Zeitler, J. Maan, W. Van der Wiel, G. Rijnders, D. Blank, and H. Hilgenkamp, *Nat. Mater.* **6**, 493 (2007).
- [13] A. Ohtomo, D. A. Muller, J. L. Grazul, and H. Y. Hwang, *Nature (London)* **419**, 378 (2002).
- [14] H. W. Jang, D. A. Felker, C. W. Bark, Y. Wang, M. K. Niranjan, C. T. Nelson, Y. Zhang, D. Su, C. M. Folkman, S. H. Baek, S. Lee, K. Janicka, Y. Zhu, X. Q. Pan, D. D. Fong, E. Y. Tsympal, M. S. Rzechowski, and C. B. Eom, *Science* **331**, 886 (2011).
- [15] P. Xu, T. C. Droubay, J. S. Jeong, K. A. Mkhoyan, P. V. Sushko, S. A. Chambers, and B. Jalan, *Adv. Mater. Interfaces* **3**, 1500432 (2016).
- [16] P. Moetakef, T. A. Cain, D. G. Ouellette, J. Y. Zhang, D. O. Klenov, A. Janotti, C. G. Van de Walle, S. Rajan, S. J. Allen, and S. Stemmer, *Appl. Phys. Lett.* **99**, 232116 (2011).
- [17] C. A. Jackson and S. Stemmer, *Phys. Rev. B* **88**, 180403 (2013).
- [18] A. S. Sefat, J. E. Greedan, G. M. Luke, M. Niewczas, J. D. Garrett, H. Dabkowska, and A. Dabkowski, *Phys. Rev. B* **74**, 104419 (2006).
- [19] D. A. McClean, K. Seto, and J. E. Greedan, *J. Solid State Chem.* **40**, 241 (1981).
- [20] See the Supplemental Material at <http://link.aps.org/supplemental/10.1103/PhysRevLett.117.106803> for experimental and modeling details, along with additional data and calculations, which includes Refs. [15,21–42].
- [21] P. Xu, D. Phelan, J. S. Jeong, K. A. Mkhoyan, and B. Jalan, *Appl. Phys. Lett.* **104**, 082109 (2014).
- [22] B. Jalan, J. Cagnon, T. E. Mates, and S. Stemmer, *J. Vac. Sci. Technol. A* **27**, 1365 (2009).
- [23] J. Son, P. Moetakef, B. Jalan, O. Bierwagen, N. J. Wright, R. Engel-Herbert, and S. Stemmer, *Nat. Mater.* **9**, 482 (2010).
- [24] B. Jalan, S. J. Allen, G. Beltz, P. Moetakef, and S. Stemmer, *Appl. Phys. Lett.* **98**, 132102 (2011).
- [25] G. Kresse and J. Furthmüller, *Phys. Rev. B* **54**, 11169 (1996).
- [26] G. Kresse and D. Joubert, *Phys. Rev. B* **59**, 1758 (1999).

- [27] P. E. Blöchl, *Phys. Rev. B* **50**, 17953 (1994).
- [28] J. P. Perdew, A. Ruzsinszky, G. I. Csonka, O. A. Vydrov, G. E. Scuseria, L. A. Constantin, X. Zhou, and K. Burke, *Phys. Rev. Lett.* **100**, 136406 (2008).
- [29] R. F. W. Bader, *Atoms in Molecules - A Quantum Theory* (Oxford University Press, Oxford, 1990).
- [30] W. Tang, E. Sanville, and G. Henkelman, *J. Phys. Condens. Matter* **21**, 084204 (2009).
- [31] S. Aggarwal and R. Ramesh, *Annu. Rev. Mater. Sci.* **28**, 463 (1998).
- [32] T. C. Kaspar, S. E. Chamberlin, M. E. Bowden, R. Colby, V. Shutthanandan, S. Manandhar, Y. Wang, P. V. Sushko, and S. A. Chambers, *J. Phys. Condens. Matter* **26**, 135005 (2014).
- [33] S. E. Chamberlin, T. C. Kaspar, M. E. Bowden, V. Shutthanandan, B. Kabius, S. Heald, D. Keavney, and S. A. Chambers, *J. Appl. Phys.* **116**, 233702 (2014).
- [34] A. A. Sokol, A. Walsh, and C. R. A. Catlow, *Chem. Phys. Lett.* **492**, 44 (2010).
- [35] T. Nakamura, Y. Linga, and K. Amezawa, *J. Mater. Chem.* **A3**, 10471 (2015).
- [36] N. L. Allan and W. C. Mackrodt, *Mol. Simul.* **12**, 89 (1994).
- [37] X. Kuang, M. A. Green, H. Niu, P. Zajdel, C. Dickinson, J. B. Claridge, L. Jantsky, and M. J. Rosseinsky, *Nat. Mater.* **7**, 498 (2008).
- [38] T. Nakamura, R. Oike, Y. Ling, Y. Tamenori, and K. Amezawa, *Phys. Chem. Chem. Phys.* **18**, 1564 (2016).
- [39] W. Xie, Y.-L. Lee, Y. S. Horn, and D. Morgan, *J. Phys. Chem. Lett.* **7**, 1939 (2016).
- [40] L. Troncoso, J. A. Alonso, and A. Aguadero, *J. Mater. Chem.* **3**, 17797 (2015).
- [41] S. A. Chambers, M. Gu, P. V. Sushko, H. Yang, C. Wang, and N. D. Browning, *Adv. Mater.* **25**, 4001 (2013).
- [42] R. L. Kurtz and V. E. Henrich, *Surf. Sci. Spectra* **5**, 182 (1998).
- [43] J. Biscaras, N. Bergeal, S. Hurand, C. Grossetête, A. Rastogi, R. C. Budhani, D. LeBoeuf, C. Proust, and J. Lesueur, *Phys. Rev. Lett.* **108**, 247004 (2012).
- [44] M. S. J. Marshall, D. T. Newell, D. J. Payne, R. G. Egdell, and M. R. Castell, *Phys. Rev. B* **83**, 035410 (2011).
- [45] S. M. Walker, F. Y. Bruno, Z. Wang, A. D. L. Torre, S. Ricco, A. Tamai, T. K. Kim, M. Hoesch, M. Shi, M. S. Bahramy, P. D. C. King, and F. Baumberger, *Adv. Mater.* **27**, 3894 (2015).
- [46] C. Lin, A. Posadas, T. Hadamek, and A. A. Demkov, *Phys. Rev. B* **92**, 035110 (2015).
- [47] S. Nemsak, G. Conti, G. K. Palsson, C. Conlon, S. Cho, J. E. Rault, J. Avila, M. C. Asensio, C. A. Jackson, P. Moetakef, A. Janotti, L. Bjaalie, B. Himmetoglu, C. G. V. de Walle, L. Balents, C. M. Schneider, S. Stemmer, and C. S. Fadley, *Appl. Phys. Lett.* **107**, 231602 (2015).
- [48] M. N. Grisolia, J. Varignon, G. S. Santolino, A. Arora, S. Valencia, M. Varela, R. Abrudan, E. Weschke, E. Schierle, J. E. Rault, J. P. Rueff, A. Barthelemy, J. Santamaria, and M. Bibes, *Nat. Phys.* **12**, 484 (2016).
- [49] L. Bjaalie, A. Janotti, K. Krishnaswamy, and C. G. Van de Walle, *Phys. Rev. B* **93**, 115316 (2016).
- [50] L. Bjaalie, D. Ouellette, P. Moetakef, T. Cain, A. Janotti, B. Himmetoglu, S. Allen, S. Stemmer, and C. Van de Walle, *Appl. Phys. Lett.* **106**, 232103 (2015).
- [51] D. G. Ouellette, P. Moetakef, T. A. Cain, J. Y. Zhang, S. Stemmer, D. Emin, and S. J. Allen, *Sci. Rep.* **3**, 3284 (2013).